

## Dipole Coupling of a Double Quantum Dot to a Microwave Resonator

T. Frey,<sup>1</sup> P. J. Leek,<sup>1</sup> M. Beck,<sup>1</sup> A. Blais,<sup>2</sup> T. Ihn,<sup>1</sup> K. Ensslin,<sup>1</sup> and A. Wallraff<sup>1,\*</sup>

<sup>1</sup>Department of Physics, ETH Zurich, CH-8093, Zurich, Switzerland

<sup>2</sup>Département de Physique, Université de Sherbrooke, Sherbrooke, Québec, J1K 2R1 Canada

(Received 6 October 2011; published 25 January 2012)

We demonstrate the realization of a hybrid solid-state quantum device, in which a semiconductor double quantum dot is dipole coupled to the microwave field of a superconducting coplanar waveguide resonator. The double dot charge stability diagram extracted from measurements of the amplitude and phase of a microwave tone transmitted through the resonator is in good agreement with that obtained from transport measurements. Both the observed frequency shift and linewidth broadening of the resonator are explained considering the double dot as a charge qubit coupled with a strength of several tens of MHz to the resonator.

DOI: 10.1103/PhysRevLett.108.046807

PACS numbers: 73.21.La, 03.67.Lx, 42.50.Pq, 73.63.Kv

Research on semiconductor quantum dots has contributed significantly to the understanding of the physics of individual charges and spins in a solid-state environment [1–3]. Typically, quantum dots are investigated by direct current (dc) transport measurements [1] or using quantum point contacts for charge sensing [4]. Here, we have realized a novel device in which a semiconductor double quantum dot is dipole coupled to a GHz-frequency high-quality transmission line resonator. This approach allows us to characterize the properties of the double dot by measuring both its dispersive and dissipative interaction with the resonator. In addition to providing a new readout mechanism, this architecture has the potential to isolate the dots from the environment and to provide long distance coupling between spatially separated dots. These features are expected to improve the potential for realizing a quantum information processor [5] with quantum dots as previously demonstrated for superconducting circuits making use of circuit quantum electrodynamics (QED) [6–8].

In quantum dots the benefits of large bandwidth and low noise detection are harnessed by using radio frequency (rf) techniques, e.g., for charge [9–12] or quantum capacitance measurements [13]. Also, a number of proposals to use microwave frequency techniques for scaling of quantum information processing architectures based on quantum dots have been put forward recently [14–17]. In this work, we have coupled charge states of a double dot to the field of an on-chip microwave transmission line resonator making use of ideas of circuit QED.

The sample we have investigated in our experiments is shown along with an electrical circuit diagram in Fig. 1. The microwave resonator [see Fig. 1(a)] is realized using a 200 nm thick aluminum coplanar waveguide on GaAs which is capacitively coupled to an input and output line to probe its transmission spectrum. The double quantum dot [see Fig. 1(c)] is positioned at an antinode of the standing wave field distribution of the resonator. The left and right dots (LD, RD) are arranged in series with respect

to the source and drain ( $S$ ,  $D$ ). They are realized on an  $\text{Al}_x\text{Ga}_{1-x}\text{As}$  heterostructure with the two-dimensional electron gas (2DEG) at a depth of about 35 nm below the surface.

A selective capacitive coupling between the two systems is mediated by a gate [resonator gate (RG)] extending from

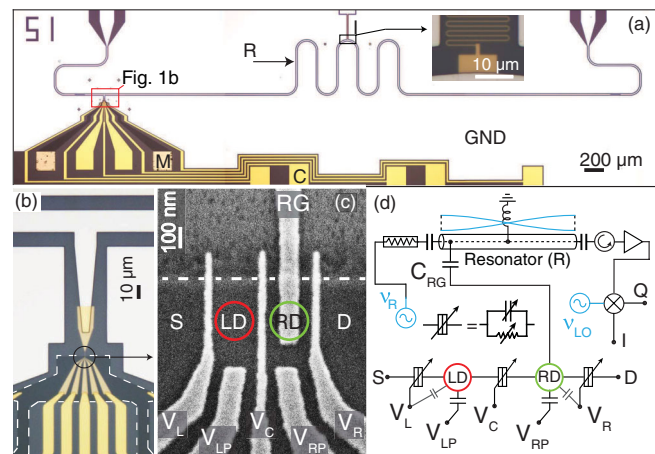


FIG. 1 (color online). (a) Optical micrograph of the microwave resonator ( $R$ ), with integrated double quantum dot, Ohmic contacts ( $M$ ), top gates ( $C$ ), ground plane ( $GND$ ), and on-chip inductor ( $I$ ). Inset: Magnified view of inductor ( $I$ ). (b) Enlarged view of the device near the double quantum dot. The mesa edge is highlighted with a dashed line. (c) Scanning electron micrograph of the gate structure defining the double quantum dot ( $LD$ ,  $RD$ ).  $RG$  marks the gate connected to the resonator,  $V_L$ ,  $V_{LP}$ ,  $V_C$ ,  $V_{RP}$ ,  $V_R$  label top gate voltages, and  $S$ ,  $D$  the 2DEG source and drain. (d) Electric circuit representation of the double quantum dot coupled to the resonator. The double quantum dot is tuned with voltages  $V_L$ ,  $V_{LP}$ ,  $V_C$ ,  $V_{RP}$ ,  $V_R$  and connected to the resonator via the capacitance  $C_{RG}$ . The resonator is driven with a microwave signal at frequency  $\nu_R$ . The transmitted signal passes through a circulator, is amplified and mixed with the local oscillator  $\nu_{LO}$  to obtain the field quadratures  $I$  and  $Q$ .

the resonator to the right quantum dot only [Fig. 1(c)]. At dc this coupling was independently confirmed by biasing the resonator through an on-chip inductor [Fig. 1(a), inset]. This coupling scheme results in a strong microwave frequency dipole interaction of the resonator with two charge states in which an electron is on either the left or right quantum dot. In order to accommodate the gate (RG), the dots are placed at the edge of a mesa (beyond which the 2DEG is etched away), used as part of the confining potential. To complete the formation of the dots, negative voltages are applied to metallic top gates [Fig. 1(a)] below which the 2DEG is then depleted.

The static potential on the dots is tuned via two plunger gate voltages  $V_{LP}$  and  $V_{RP}$ . To allow electron transport, the two dots are connected to each other and to the source ( $S$ ) and drain ( $D$ ) contacts through tunnel barriers, tunable by applied voltages  $V_L$ ,  $V_C$ , and  $V_R$  [see Figs. 1(c) and 1(d)]. Because of finite capacitive coupling, these tunnel barrier gates also tune the dot potentials with a similar lever arm as the plunger gates. Finally, we apply a coherent microwave signal at frequency  $\nu_R$  to the resonator ( $R$ ) to extract the amplitude  $A$  and phase  $\phi$  of the transmitted signal from the measured field quadratures  $I$  and  $Q$ , as  $Ae^{i\phi} = I + iQ$ , in a heterodyne detection scheme [6]. The experiments are performed in a dilution refrigerator with a base temperature of approximately 10 mK.

We first investigated the dc transport properties of the double quantum dot [see Fig. 2(a)] by applying a source-drain voltage of  $V_{SD} \approx 50 \mu\text{V}$ . To change the electrostatic potentials on the quantum dots, the voltages  $V_L$  and  $V_R$  are varied while all other gate voltages are fixed. We observe a hexagon charge stability pattern, which is characteristic for electron transport through double quantum dots [2]. Within each hexagon, the number of electrons ( $N, M$ ) in the dots is fixed. At the triple points, where three charge states are degenerate, charge transport is energetically possible and a conductance resonance is observed. The current observed along four of the hexagon boundaries is caused by cotunneling or molecular orbital states [18]. At the two hexagon boundaries indicated by red arrows in Fig. 2(a) at which no dc current was measured, two quantum dot charge states with the same total number of electrons are degenerate [2]. Along this direction [Fig. 2(a)], the mean energy  $\epsilon$  of the two quantum dots is tuned with respect to the chemical potentials of the leads. The energy detuning  $\delta$  between the charge states of the quantum dots is changed along a second axis indicated in the same figure. The charging energies of both quantum dots are  $E_C \approx 1 \text{ meV} \approx h \times 240 \text{ GHz}$  as extracted from Coulomb diamond measurements. Both quantum dots contain on the order of 100 electrons. An electron temperature of  $T_e \lesssim 135 \text{ mK}$  is estimated from Coulomb resonance linewidths [1].

The microwave resonator, designed as in Ref. [19], has a fundamental frequency  $\nu_0 \approx 6.755 \text{ GHz}$  and a loaded quality factor [20]  $Q_L \approx 2630$  corresponding to a decay

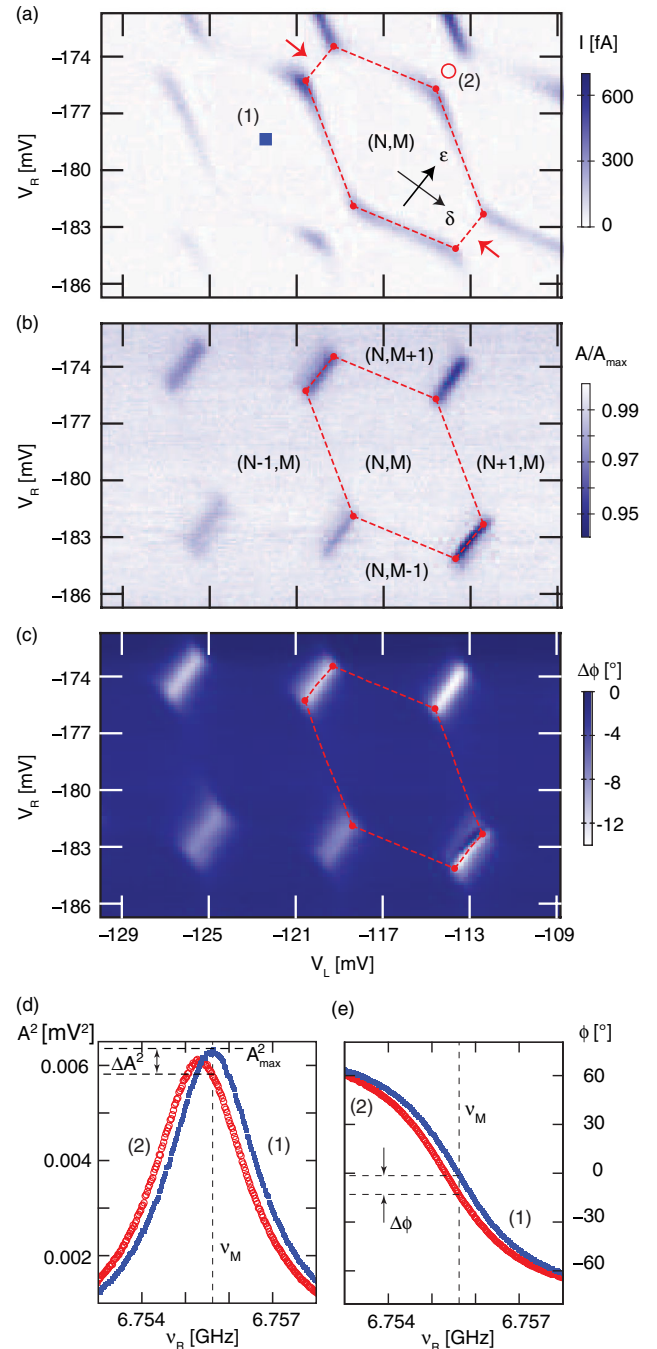


FIG. 2 (color online). (a) Measurement of the direct current through the double quantum dot versus  $V_L$ ,  $V_R$  (no microwave signal applied). A small background current is subtracted from each horizontal line of the data set. The dashed line outlines a region with fixed electron number  $(N, M)$ . The  $\epsilon$  and  $\delta$  axes indicate the direction of the mean and the detuning energy of the two quantum dots. (b) Resonator transmission amplitude at fixed measurement frequency  $\nu_M$  in the same gate voltage range as in (a). The red dashed lines highlight the same hexagon as in (a). (c) Transmission phase change with respect to  $\nu_M$ , gate voltages as in (a). Red dashed lines as in (a). (d),(e) Measured transmission spectra of the microwave resonator at positions (1) (blue rectangles) and (2) (red open points), indicated in (a). (d) Transmission amplitude and (e) phase.

rate  $\kappa/2\pi \approx 2.6$  MHz, measured with all gates grounded such that no quantum dots are formed. The resonator is approximately prepared in its ground state with average thermal photon number  $n < 1$  using appropriate filtering and attenuation in the microwave lines.

When the double quantum dot is formed by applying negative gate voltages, we find that the resonator frequency and linewidth are sensitively dependent on these voltages. In Figs. 2(d) and 2(e) the amplitude and phase of the microwaves transmitted through the resonator are shown for the two voltage settings indicated with (1) and (2) in Fig. 2(a). In the two cases, different resonance frequencies and maximum transmission amplitudes are observed. In both configurations (1) and (2), transport is blocked between the leads due to Coulomb blockade. However, in (1), the electron number in both dots is fixed, whereas in (2), a pair of left and right dot charge states are degenerate and hybridized states are formed. The modified resonator response indicates that the double dot couples with significant interaction strength to the resonator. Note that here, and in all further microwave transmission measurements, no source or drain bias is applied to the double dot.

For the same gate voltage ranges as shown in Fig. 2(a), we have measured the dependence of the amplitude and phase of microwaves transmitted through the resonator at fixed probe frequency  $\nu_M$  [Figs. 2(b) and 2(c)]. We observe a clear reduction of the transmission amplitude and a change of the transmission phase at the charge triple points and along the interdot charge transfer lines connecting pairs of triple points. However, no change of signal is observed along the cotunneling lines and in the regions with fixed electron numbers in both dots. In this parameter regime, a resonator response only occurs at gate voltages at which charges are transferred between the two dots leading to a dipole coupling to the resonator. Details of the coupling mechanism are discussed below. We also note that the charge stability diagram in the microwave measurement is well aligned in gate voltage with the one in the transport measurements as indicated by the hexagon patterns shown as red dashed lines in Figs. 2(a)–2(c). Similar stability diagrams have been observed over a range of more than 10 electrons in both the left and right dot, including gate voltage settings at which the tunneling rates were so small that the dc current through the double quantum dot could not be detected in direct transport measurements ( $I \lesssim 80$  fA).

We have examined in more detail the phase of the transmitted microwaves in the vicinity of one particular interdot charge transfer line, for different values of interdot tunnel coupling energy  $t$ , tuned using  $V_C$ . More negative  $V_C$  gives a smaller  $t$ . In order to discuss the experimental data as clearly as possible, we assume in the following that  $2t$  can be larger or smaller than the resonator energy  $h\nu_0$ . We justify this assumption after the presentation of the data with a quantitative model. The two plunger gates  $V_{LP,RP}$  are

swept (rather than  $V_{L,R}$ ), to minimize the change of the tunnel rates to the leads, and  $V_{L,R}$  are set such that the tunneling rates to the leads are too small to measure dc transport. The data shown in the left (right) column of Fig. 3 were acquired with the center gate set to  $V_C = -120$  mV ( $-119$  mV) corresponding to  $2t$  smaller (larger) than  $h\nu_0$ , as discussed below. Despite the small change in  $V_C$  between the two measurements, the two phase signals are clearly different. Note that the detuning  $\Delta = \delta/h - \nu_0$  is changed over a frequency range larger than the resonator frequency  $\nu_0$  using the plunger gate voltages. In Fig. 3(a), two regions of negative phase shift are observed on either side of a region of positive phase shift along the interdot charge transfer line. In Fig. 3(b) however, a single region of negative phase shift is seen, similar to the features shown in Fig. 2(c). Negative (positive) phase shifts translate directly to negative (positive) resonance frequency shifts [see Figs. 2(d) and 2(e)].

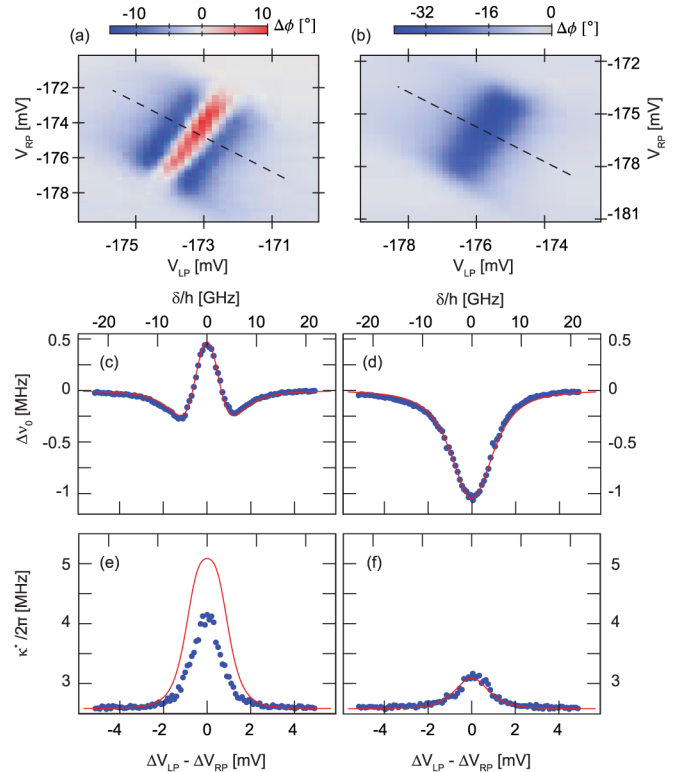


FIG. 3 (color online). (a) Measured transmission phase as a function of  $V_{LP}$  and  $V_{RP}$  at  $V_C = -120$  mV (with  $2t < h\nu_0$ , as extracted from simulations). Black dashed line indicates axis swept in (c),(e). (b) Transmission phase measured at  $V_C = -119$  mV (with  $2t > h\nu_0$  from simulation). Black dashed line indicates axis swept in (d),(f). (c),(d) Measured resonator frequency shift  $\Delta\nu_0$  (blue points) along the axes shown in (a) and (b), respectively. (e),(f) Broadened resonator linewidth  $\kappa^*$  (blue points) measured along the axes shown in (a) and (b), respectively. Solid red lines in (c)–(f) are results of numerical simulations.

To characterize the interaction between the two systems in more detail we have measured the full resonator transmission spectrum for a set of gate voltages swept across the interdot charge transfer line. For all parameters, the measured spectra are well approximated by a single Lorentzian line. The extracted frequency shift  $\Delta\nu_0$  relative to  $\nu_0$  and the extracted linewidth  $\kappa^*$  are plotted in Figs. 3(c)–3(f) along the black dashed line in (a),(b) for the two different interdot tunnel coupling strengths. In agreement with the data in Figs. 3(a) and 3(b), for  $2t < h\nu_0$  both negative and positive frequency shifts are observed in the left panel whereas for  $2t > h\nu_0$  only negative frequency shifts are seen in the right panel. In both cases an increase in  $\kappa^*$  is observed when the energy difference between two charge states is close to the resonator frequency.

In the following we compare these observations in more detail with results obtained from a master equation simulation taking both coherent interaction between the double dot and the resonator and decoherence into account. We model our device as a charge qubit [21] coupled to a quantized harmonic oscillator considering a Hamiltonian

$$H = h\nu_0\left(\hat{n} + \frac{1}{2}\right) + \frac{h\nu_q}{2}\hat{\sigma}_z + \hbar g \sin\theta(\hat{a}^\dagger\hat{\sigma}^- + \hat{a}\hat{\sigma}^+), \quad (1)$$

of the Jaynes-Cummings type [14] with  $\nu_q = \sqrt{\delta^2 + 4t^2}$  and  $\sin\theta = 2t/\sqrt{\delta^2 + 4t^2}$ . Here  $\delta$  is the detuning energy between the qubit states,  $\hbar g$  the coupling energy between the resonator and the qubit,  $\hat{n} = a^\dagger a$  the photon number operator, and  $\sigma^{+/-}$  and  $\sigma_z$  the Pauli operators for the qubit. In Fig. 4, the two lowest eigenenergies of the coupled system are shown schematically as a function of  $\delta$  for the two relevant cases (a)  $2t < h\nu_0$  and (b), (c)  $2t > h\nu_0$ . In the presence of an interaction of strength  $g$ , the bare resonator frequency  $\nu_0$  (dashed green line) and the bare charge qubit transition frequency  $\nu_q$  (dotted red line) are coupled by the interaction to give the solid black lines shown in Fig. 4. In the absence of decoherence this model displays an avoided level crossing at  $\nu_q = \nu_0$  known as the vacuum Rabi mode splitting [22].

Using a Markovian master equation approach [22] to obtain a steady-state numerical solution of the Hamiltonian Eq. (1) including resonator and qubit energy relaxation and qubit dephasing [23], we are able to explain the characteristic features of the data shown in Figs. 3(c)–3(f). Indeed, using the measured values of  $\nu_0$  and  $\kappa$ , choosing an energy relaxation rate at  $\delta \gg t$  of  $\gamma_1/2\pi = 100$  MHz typical for charge qubits [24], and using a constant factor related to the difference between lever arms of the left and right quantum dot to convert gate voltage to detuning energy  $\delta$ , we find that all simulations are in reasonable agreement with the data, see red lines in Figs. 3(c)–3(f). To achieve this agreement, we consider a coupling strength of  $g/2\pi = 50$  MHz for all data sets but take a tunneling energy  $2t/h = 6.1$  GHz  $< \nu_0$  and a pure dephasing rate

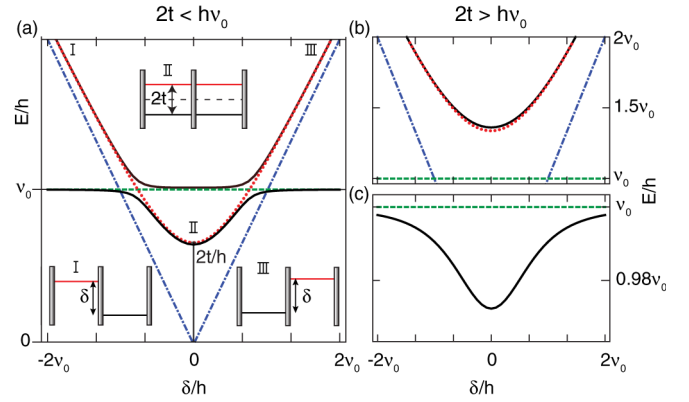


FIG. 4 (color online). (a) Schematic of the two lowest eigenenergies of the coupled system for  $2t < h\nu_0$ . Horizontal green dashed line indicates the bare resonator frequency  $\nu_0$ . Red dotted line shows the bare transition frequency  $\nu_q$  between the double dot charge states. The two sloped blue dash-dotted lines indicate the detuning  $\delta$ . Insets I and III: Schematic of the two double dot charge states detuned by energy  $\delta$ , in the limit  $\delta \gg t$ . Inset II: Schematic of the hybridized charge states in the double quantum dot, split by  $2t$  at  $\delta = 0$ . (b) Transition energy of the charge qubit for  $2t > h\nu_0$  in the presence of the nearby resonator. Dashed and dotted lines as in (a). (c) Resonator frequency in the presence of the nearby charge qubit transition for the same case as in (b).

$\gamma_\phi/2\pi = 3.3$  GHz at  $\delta \gg t$  for Figs. 3(c) and 3(e) and  $2t/h = 9$  GHz  $> \nu_0$ , and a smaller value of  $\gamma_\phi/2\pi = 0.9$  GHz at  $\delta \gg t$ , for Figs. 3(d) and 3(f). The order of magnitude of the values found for the dephasing rates at  $\delta = 0$  within our model are comparable to those found in other quantum dot charge qubit experiments [21]. The estimated value of  $g$  considered here agrees well with an estimate obtained from the capacitive coupling between qubit and resonator. Since the qubit dephasing rate  $\gamma_\phi$  is in both cases significantly larger than the coupling strength  $g$ , we do not observe a vacuum Rabi mode splitting, but rather a single spectral line broadened and shifted from its original frequency. At detunings  $\Delta$  between the double dot charge states and resonator that are on the order of or larger than the qubit linewidth, we can clearly observe frequency shifts induced by the nonresonant coupling. We conclude that the size of the observed shifts is in good agreement with our model.

For this set of extracted parameters, we also note that the measured linewidth [Fig. 3(e)] is lower than the one found from our calculation. This discrepancy is potentially due to the frequency dependence of the noise that leads to decoherence which is not considered in the Markovian model. To double-check the conclusions from our simulations, we have confirmed both experimentally and in simulation that the results in Fig. 3 are independent of changes in the resonator population due to coherent or thermal fields with a mean occupation of below approximately 10 photons. This observation is reasonable, since the large

dephasing rate makes the rather small changes due to the nonlinearities arising at larger photon numbers [25] unobservable in the current experiments.

In summary, we have successfully demonstrated the dipole coupling of a double quantum dot to an on-chip superconducting microwave resonator and probed the double dot charge stability diagram by measuring resonator frequency shifts. Two different characteristic regimes with interdot tunnel couplings above or below the resonator frequency could be observed and explained. This demonstrated that our architecture offers a new way to probe semiconductor quantum systems in the microwave regime, and may be used, for example, for high energy-resolution measurements of double quantum dots [26] and fast time-resolved measurements, in addition to being a promising platform for potentially scalable hybrid solid-state quantum information processing. The presented scheme could be extended to other material systems, manipulating and reading out spin qubits [3] and coupling them to a microwave resonator using either ferromagnetic leads [27] or spin orbit effects [28].

We thank C. Rössler, T. Müller, and D. Loss for valuable discussions, C. Lang, P. Studerus, T. Schoch, and V. Tshitoyan for their contributions to the project. This work was supported financially by EU IP SOLID, by the Swiss National Science Foundation through the National Center of Competence in Research “Quantum Science and Technology” and by ETH Zurich. A. B. was supported by NSERC, the Alfred P. Sloan Foundation, and CIFAR.

*Note added.*—Recently, we became aware of a related work [29] with a single quantum dot.

---

\*andreas.wallraff@phys.ethz.ch

- [1] L. P. Kouwenhoven *et al.*, in *Mesoscopic Electron Transport*, edited by L. L. Sohn, L. P. Kouwenhoven, and G. Schön, NATO ASI, Ser. E, Vol. 345 (Kluwer, Dordrecht, 1997), pp. 105–214.  
 [2] W. G. van der Wiel *et al.*, *Rev. Mod. Phys.* **75**, 1 (2002).

- [3] R. Hanson, L. P. Kouwenhoven, J. R. Petta, S. Tarucha, and L. M. K. Vandersypen, *Rev. Mod. Phys.* **79**, 1217 (2007).  
 [4] M. Field *et al.*, *Phys. Rev. Lett.* **70**, 1311 (1993).  
 [5] M. A. Nielsen and I. L. Chuang, *Quantum Computation and Quantum Information* (Cambridge University Press, Cambridge, England, 2000).  
 [6] A. Wallraff *et al.*, *Nature (London)* **431**, 162 (2004).  
 [7] R. J. Schoelkopf and S. M. Girvin, *Nature (London)* **451**, 664 (2008).  
 [8] J. Majer *et al.*, *Nature (London)* **449**, 443 (2007).  
 [9] W. Lu, J. Zhongqing, L. Pfeiffer, K. W. West, and A. J. Rimberg, *Nature (London)* **423**, 422 (2003).  
 [10] D. J. Reilly, C. M. Marcus, M. P. Hanson, and A. C. Gossard, *Appl. Phys. Lett.* **91**, 162101 (2007).  
 [11] M. C. Cassidy *et al.*, *Appl. Phys. Lett.* **91**, 222104 (2007).  
 [12] T. Müller *et al.*, *Appl. Phys. Lett.* **97**, 202104 (2010).  
 [13] K. D. Petersson *et al.*, *Nano Lett.* **10**, 2789 (2010).  
 [14] L. Childress, A. S. Sørensen, and M. D. Lukin, *Phys. Rev. A* **69**, 042302 (2004).  
 [15] J. M. Taylor *et al.*, *Nature Phys.* **1**, 177 (2005).  
 [16] G. Burkard and A. Imamoglu, *Phys. Rev. B* **74**, 041307(R) (2006).  
 [17] J. M. Taylor and M. D. Lukin, arXiv:cond-mat/0605144.  
 [18] S. Gustavsson *et al.*, *Phys. Rev. B* **78**, 155309 (2008).  
 [19] T. Frey *et al.*, *Appl. Phys. Lett.* **98**, 262105 (2011).  
 [20] M. Göppl *et al.*, *J. Appl. Phys.* **104**, 113904 (2008).  
 [21] T. Hayashi, T. Fujisawa, H. D. Cheong, Y. H. Jeong, and Y. Hirayama, *Phys. Rev. Lett.* **91**, 226804 (2003).  
 [22] D. F. Walls and G. J. Milburn, *Quantum Optics* (Springer-Verlag, Berlin, 2008).  
 [23] R. J. Schoelkopf *et al.*, in *Quantum Noise in Mesoscopic Physics*, edited by Y. V. Nazarov (Kluwer, Dordrecht, 2003), pp. 175–203.  
 [24] J. R. Petta *et al.*, *Phys. Rev. Lett.* **93**, 186802 (2004).  
 [25] L. S. Bishop *et al.*, *Nature Phys.* **5**, 105 (2008).  
 [26] P. Q. Jin, M. Marthaler, J. H. Cole, A. Shnirman, and G. Schön, *Phys. Rev. B* **84**, 035322 (2011).  
 [27] A. Cottet and T. Kontos, *Phys. Rev. Lett.* **105**, 160502 (2010).  
 [28] M. Trif, V. N. Golovach, and D. Loss, *Phys. Rev. B* **77**, 045434 (2008).  
 [29] M. R. Delbecq *et al.*, *Phys. Rev. Lett.* **107**, 256804 (2011).